Lumen charge governs ion transport in β-barrel nanopores

Simon Finn Mayer[1,2,†], Marianna Fanouria Mitsioni[1,2,†], Lukas van den Heuvel[2], Paul Robin[3], Nathan Ronceray[1], Maria Josefina Marcaida[2], Luciano A. Abriata[2], Lucien F. Krapp[2], Jana S. Anton[2], Sarah Soussou[1], Justin Jeanneret-Grosjean[1], Alessandro Fulciniti[2], Alexia Möller[2], Sarah Vacle[2], Lely Feletti[1], Henry Brinkerhoff[4], Andrew H. Laszlo[4], Jens H. Gundlach[4], Theo Emmerich[1], Matteo Dal Peraro[2,#,*], Aleksandra Radenovic[1,#,*]

[1] Institute of Bioengineering, School of Engineering, Swiss Federal Institute of Technology Lausanne, Lausanne, Switzerland
[2] Institute of Bioengineering, School of Life Sciences, Swiss Federal Institute of Technology Lausanne, Lausanne, Switzerland
[3] Institute of Science and Technology Austria, Klosterneuburg, Austria
[4] Department of Physics, University of Washington, Seattle, United States of America
*To whom correspondence should be addressed; e-mail:, matteo.dalperaro@epfl.ch,aleksandra.radenovic@epfl.ch
[†] These authors contributed equally
[#] These authors jointly supervised this work

Abstract

β-barrel nanopores are involved in crucial biological processes, from ATP export in mitochondria to bacterial resistance, and represent a promising platform for emerging sequencing technologies. However, the fundamental principles governing ion transport across these nanopores remain poorly understood due to their extreme confinement and heterogeneous lumen charge. In this study, we integrate experimental, numerical, and theoretical approaches to elucidate ion transport mechanisms in these biological nanopores. We identify and characterise two distinct nonlinear phenomena: open-pore rectification and gating. Through extensive mutation analysis of aerolysin and α-hemolysin nanopores, we demonstrate that open-pore rectification is caused by ionic accumulation driven by the distribution of lumen charges. Additionally, we provide converging evidence suggesting that gating is controlled by electric fields pulling on lumen charges and controlled by local structural deformations. Our findings pave the way for the design of optimised biosensors as well as highly tunable and compact ionic memristors and diodes for biological computing applications. They also establish a rigorous framework for the characterization of biological ion transport processes.

Introduction

Pore-forming membrane proteins are biological nanofluidic channels enabling the regulated or free passage of molecules and ions across membranes. They are essential for information transmission, import and export, as well as attack and defence of cells and organisms[1]. Out of their biological context, they have been repurposed as sensors for probing a diverse range of molecules[2–9]. These sensors are known as biological nanopores and have been commercialised for low-cost, long-read DNA sequencing[8], a first demonstration of their potential for societal impact. The technique relies on measuring variations of the ionic current induced by the passage of an analyte molecule through the pore. Even though nanopore sequencing has achieved societal impact, ionic motion through biological nanopores still awaits proper rationalisation. It is well known that ion transport through such biological channels is highly nonlinear[10,11]. In particular, the ionic current through such pores can be polarity-dependent, an effect known as rectification[12–14], and it can abruptly decrease, a phenomenon referred to as gating[11,15–23]. The mechanisms underlying such nonlinearities, particularly the role of lumen charge, remain poorly understood, hindering further progress in biological nanopore sensing technologies. This contrasts with solid-state nanofluidics, where advances in nanofabrication and theoretical modelling have enabled in-depth rationalisation of ion transport in confinement, taking into account their surface properties[24]. For biological pores, such characterization is more challenging due to their sub-nanometric radius as well as their heterogeneous surface charge. Understanding ion transport in these pores is nonetheless of paramount importance due to their pivotal role in living organisms as well as their potential for disruptive technology.

In this work, we aim at rationalising ion transport in biological pores taking into account the complexity of their lumen charge as well as their mechanical properties. We then harness this knowledge to uncover the physical origin of biological nanopore gating. We focus on multimeric β-barrel-forming nanopores widely used in the nanopore field (S.Figure 1) such as the toxins aerolysin, and α-hemolysin (α-HL) as well as *Mycobacterium smegmatis* porin A (MspA). They are to be distinguished from smaller highly specific ion channels that often undergo conformational changes to enable or disable transport of a specific species of ion[10]. To capture the complexity of the lumen charge, we study the dependence of gating on 26, 6 and 5 different mutants of aerolysin, α-HL and MspA, respectively. Such pores have constriction diameters between around 1 and 1.4 nm and a length of roughly 10 nm[9,25]. Our study combines single-pore and ensemble transmembrane ion transport measurements,

biophysical modelling combining Poisson-Boltzmann electrostatics and nanopore mechanics, atomistic molecular dynamics (MD) simulations and cryo-electron microscopy (cryo-EM) characterization. We show how the charge landscape of the biological pore lumen controls the open-pore ion transport across them. We then present evidence that this landscape impacts voltage-induced mechanical deformations resulting in gating.

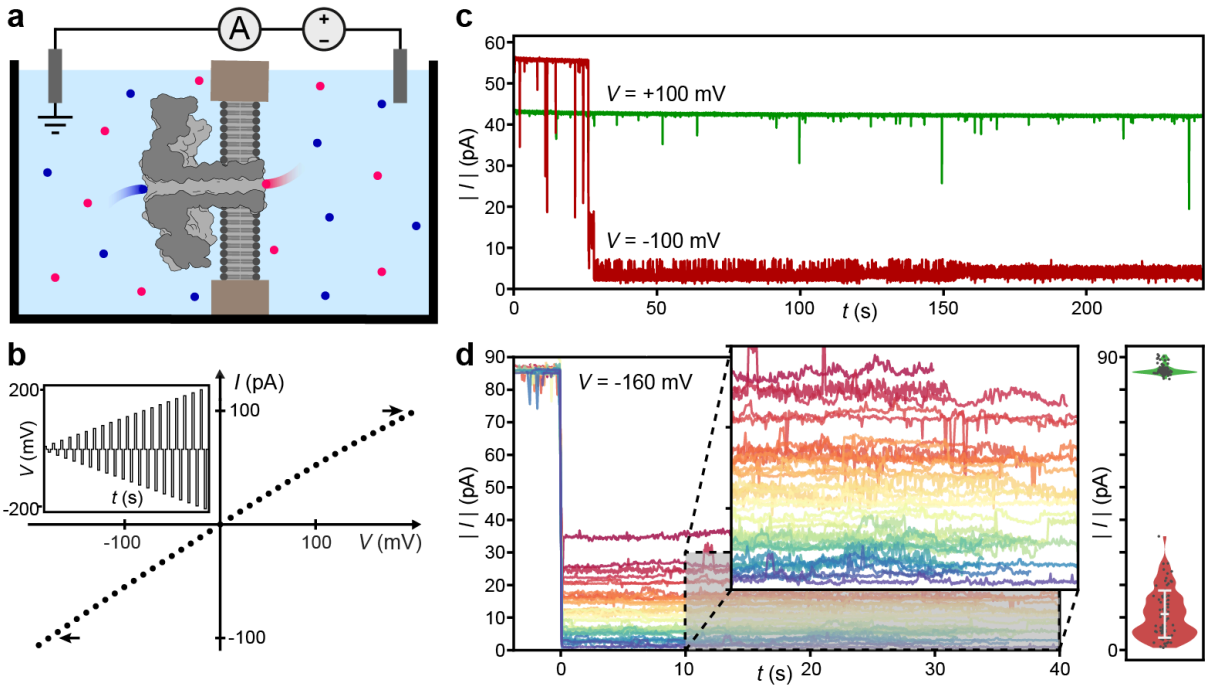

Figure 1 | Complexity and diversity of ion transport in single aerolysin pores. a Not-to-scale schematic of the experimental setup. A lipidic membrane separating two reservoirs filled with electrolyte (cations are shown in blue, anions are shown in red) with a single aerolysin pore incorporated, the current through the pore is measured via Ag/AgCl electrodes. **b** Typical single pore *IV* curve where the current of the open-pore is measured at different voltages consecutively. A slight rectification is visible and indicated through arrows at ±100 pA. The inset shows the voltage trace that can be used to acquire such data. **c.** Absolute current over time traces at constant potential of a single aerolysin nanopore. The same pore is measured first at 100 mV (green) and then at -100 mV (red) for 240 seconds. Rectification is clearly visible as the absolute current is higher at -100 mV. At 100 mV the measured current is constant while at -100 mV the current decreases spontaneously, this behaviour is referred to as gating. **d (left)** 39 gating traces recorded for a single aerolysin pore at -160 mV, coloured by current, showing the diversity of gating states associated with different current levels. **(right)**: violin plot of current levels measured in 4 different single pores probing the gating at 160 mV. Each randomly offset point in the violin plot represents the average of the gating or open-pore current of one gating trace. The white denotes the average and standard deviation of the average closed-state currents. The large closed-state current variation relative to the open-pore current variation points to a stochastic phenomenon. All experiments are done at 1 M KCl buffered to pH 6.2 with 10 mM phosphate.

Open-pore rectification and gating: two distinct nonlinearities

To show the complexity of ion transport in biological pores, we start by studying the response of single aerolysin pores to a constant applied potential. Figure 1a illustrates our experimental setup, where a single nanopore is embedded into a lipid membrane separating two electrolytic solutions containing two silver/silver-chloride electrodes. A voltage bias is applied on the electrodes and the resulting ionic current across the nanopore is measured. The membranes are freshly folded[15] or painted[26] and, by fine tuning the nanopore concentration, we have control over the number of nanopores inserted in the membrane.

When probed at different voltages for a few seconds at a time in order to obtain the *IV* curve, a small rectification is observed (Figure 1b), meaning that the pore conductance at +100mV differs from that at -100 mV. We then applied a constant potential of both opposite signs for a few minutes in order to monitor the pore stability (Figure 1c). We observed that after a few tens of seconds, the negative current trace suddenly reduces by more than 90%. This abrupt decrease is the signature of gating[11] and it hinders analyte sensing applications where a stable baseline current trace is required[9,27]. Over the last decades, a number of experimental studies aimed at characterising and understanding the gating phenomenon in β-barrel biological nanopores have been conducted and several hypotheses have been proposed, most convincingly conformational changes, among others[15–18,11,19–23]. However, no compelling evidence has been presented yet. Aerolysin, as well as other biological pores, thus exhibit two distinct nonlinearities. The first takes the form of an open-pore rectification, while the second is a delayed, sharp, and polarity-dependent decrease in current, referred to as gating.

To investigate this behaviour further we recorded the same single aerolysin nanopore over several hours and found that despite the fact that the current reduces to a discrete state or switches between several discrete states, these states are diverse in their average current. We proceeded as follows: we applied a voltage of -160mV until the pore gated, then removed the applied voltage after a few tens of seconds, before reapplying the same -160mV bias. As shown in Figure 1d displaying 39 traces it is rare that the same state is observed in different gating events. Overall, we recorded 4 different pores – no clearly defined separated states emerged from this larger sample (Figure 1d) The low throughput of single-pore direct current (DC) measurements combined with the stochastic and diverse nature of gating makes this approach unsuitable for extensive characterization of the phenomenon. This calls for a novel approach to understand this phenomenology.

Biological pores exhibit history-dependent conductivity as they switch from the open to the closed-state after approximately 30 seconds in the displayed trace (Figure 1c). In other words they behave as resistors with an internal variable sensitive to the applied voltage. Such devices are called memristors (resistors with memory). Intensively studied in electronics[28–30], memristive behaviour has recently been reported in solid-state[31–34] and biological nanofluidic devices[20,21]. As is standard in memristor studies, we quantified the similarly nonlinear dynamics of our biological nanopores through AC measurements of the *IV* curves.

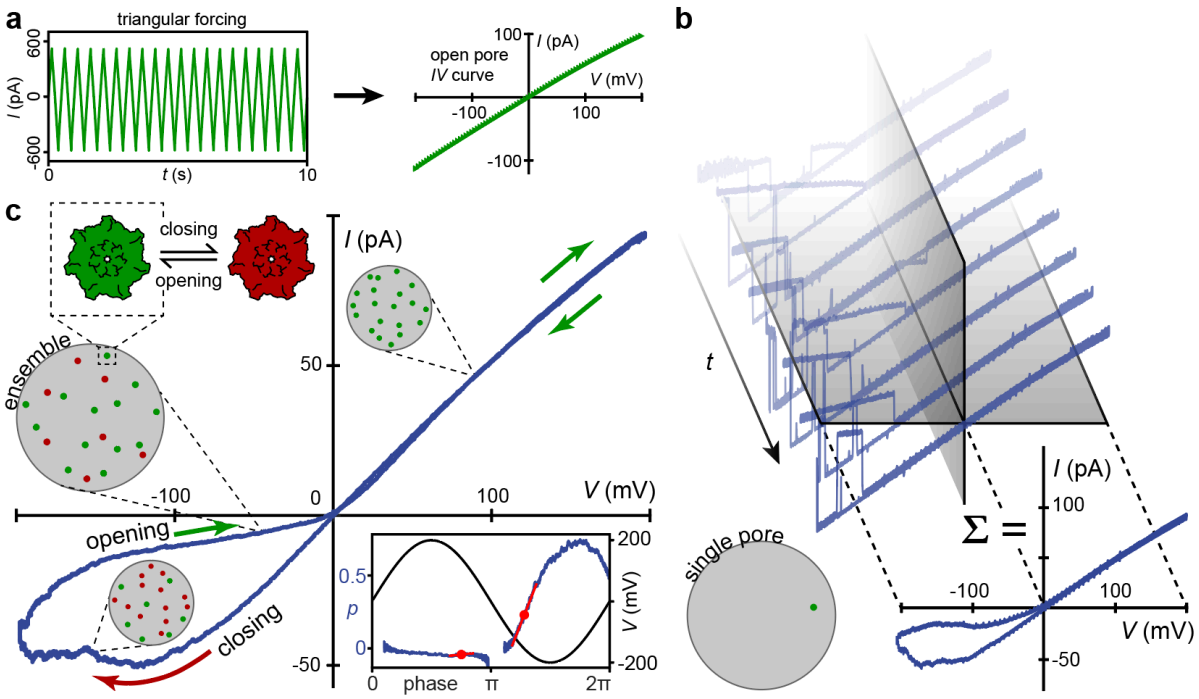

Figure 2 | Methodology for the characterization of nonlinearities using time-varying voltage drop across single and multi-pore membranes. a Triangular forcing at 2 Hz, 200 mV, with six aerolysin nanopores used to extract the single open-pore *IV* curve. **b** *IV* characteristics of a single aerolysin nanopore in the lipid membrane measured with sinusoidal potential (0.1 Hz). 50 consecutive cycles are summed to retrieve the smooth hysteresis loop. **c** *IV* characteristics of 26 pores in the same membrane showing the smooth hysteresis loop (0.1 Hz). Pores in the membrane are closing and opening in a voltage-dependent way, giving rise to the hysteresis loop. Arrows indicate the direction of the sweep. The inset shows how we quantify gating by dividing the measured current by the single open-pore *IV* to retrieve the closed-state probability *p*, the solid black line shows the sinusoidal voltage. The calculation of *p* is ill-defined close to π, resulting in a discontinuous line in the probability plot which did not affect our conclusions (see M&M Section 4). The maximum slope indicated by the red lines and dots corresponds to k_X/ω for both polarities where k_X is the closing rate and ω the forcing frequency. All experiments were conducted at 1 M KCl buffered with 10 mM phosphate to pH 6.2.

Characterization of open-pore rectification and gating with time-varying voltage

We used a periodic potential bias to measure and quantify both the open-pore rectification and the gating in a robust and rapid manner. For the open-pore rectification, triangular forcing was applied across a single pore at a frequency high enough for gating-free cycles to be observed (~Hz) (Figure 2a). The rectification of a given pore is then quantified as a unitless value between -1 and 1 by the rectification factor $\beta = (I_+ - |I_-|)/(I_+ + |I_-|)$ where $I_\pm = I(V = \pm 100\ \text{mV})$. To investigate gating, we chose a low-frequency sinusoidal span to maximise the time spent at higher voltages and therefore the closed-state probability.

When this low-frequency voltage was applied, the single aerolysin pore switched between open and closed-states in the previously described stochastic, voltage-dependent way, the pore remained in the open-state at positive biases and closed at negative applied biases. The stochasticity resulted in significant variations of the *IV* curve at negative voltage between cycles (Figure 2b). When 50 consecutive cycles of the same pore are averaged the characteristic memristive hysteresis becomes clearly visible, in the form of a loop in the *IV* curve (Figure 2b). Analysing this stochastic phenomenon thus requires a high number of repetitions in order to extract its average behaviour. We found that measuring a single sweep of multiple pores in the membrane at the same time (ensemble average) (Figure 2c) results in the same response as the time average performed in Figure 2b. Contrary to previous interpretations[35], this proves that gating is ergodic. Furthermore, using phenomenological modelling, we were able to capture the transition from single pore to collective behaviour. The conductance of the ensemble membrane can be expressed from single pore gating dynamics through the following equation:

$$G(V,t) = N_p \cdot [(1 - p(t)) \cdot G_O(V) + p(t) \cdot G_X(V)] \qquad \text{Equation 1}$$

where N_p is the number of pores, $p(t)$ is the time-dependent probability for the pores to be closed and $G_{O/X}(V)$ refers to the single-pore voltage-dependent conductance in the open/closed-state, respectively. Ensemble measurement *IV* curves were normalised by the single pore *IV* curve in a voltage window where no gating takes place which yields N_p (details in S.Section 3). We could reliably conduct single-pore measurements where the pore remains open for a full cycle (Figure 2b), yielding $I_O = G_O(V(t)) \cdot V(t)$. Thus, relying on the observation from single-pore measurements that the gated state conducts 14% of the open-pore current on average ($G_x \approx 0.14 \cdot G_O$, Figure 1d) we can invert equation 1 to obtain $p(t)$. The measured probability $p(t)$ is governed by the following rate equation:

$$\frac{dp}{dt}(t) = -k_O(V,t) \cdot p(t) + k_X(V,t) \cdot (1 - p(t)) \qquad \text{Equation 2}$$

By using constant voltage pulses, we were able to extract the opening rate k_O and closing rate k_X at different voltage biases and accurately fit the ensemble memristive hysteresis across various frequencies (S.Figure 2).

Following this analysis, we combine ensemble and single-pore measurements in order to quantify gating in various different experimental conditions. S.Figure 2 shows that when the pores start closing above a critical voltage V_c, the opening rate is zero. This means that for $|V| > V_c$ the first term in equation 2 is dropped. Therefore the maximum slope of *p(t)* is simply the rate of closing k_X (Figure 2c inset), that we chose to quantify gating.

Overall, ensemble measurements present three major advantages over single pore measurements. They offer a high throughput and a large signal to noise ratio, and have a higher success rate since it is much easier to incorporate many pores in a membrane than one. Thus, relying on the ergodicity of the stochastic ion transport through aerolysin pores, ensemble measurements enable the high-throughput quantification of gating. Our alternating current (AC) measurements inspired by the memristor literature also allows us to quantify both open-pore rectification and gating independently and reliably by varying the voltage frequency. We now harness this technique to understand the role of pore lumen charge on ion transport in biological pores. To achieve this, we tuned the lumen charge at deterministic locations inside the different pores by creating a wide mutant library.

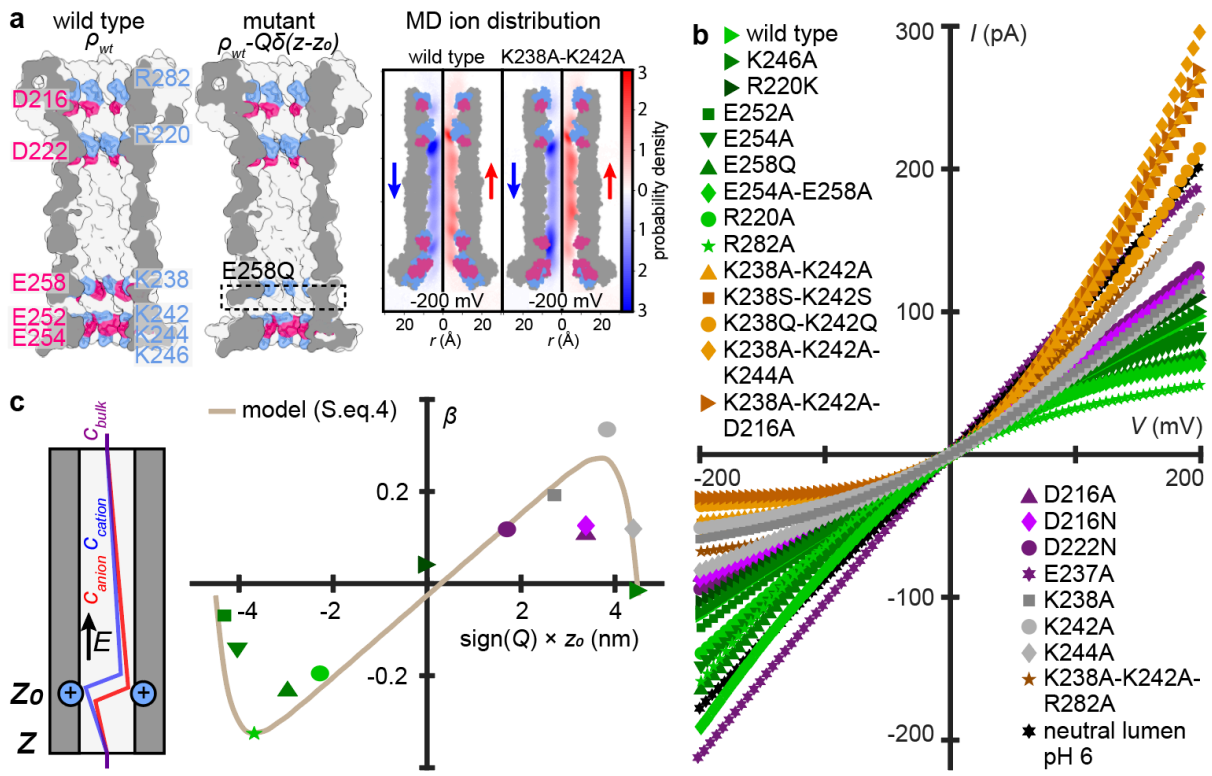

Figure 3 | Characterization of open-pore current rectification using a wide library of aerolysin mutants. a (left) aerolysin wild type (wt) and mutant E258 showing the deletion of a charged residue; **(right)** ion radial probability distributions (blue for K+, red for Cl-) measured on the MD simulations of aerolysin wt and mutant K238A-K242A at -200 mV. **b** Open-pore *IV* curves of several mutants of aerolysin showcasing the different degrees of rectification tuned by the lumen charge (1 M KCl, 10 mM phosphate pH 6.2, 1 Hz). **c (left)** schematic representation of mutant E258Q in the rectification model. The deletion of E258 which is negatively charged is represented as the addition of a fixed positive charge in the pore's energy landscape, leading to ion accumulation downstream of the fixed charge. **(right)** rectification factor *β* as function of the sign and position of the charge deleted after mutation. Solid curve: theoretical model (S.Equation 4)

Open-pore rectification of aerolysin is regulated by lumen charge.

Mutations allow us to easily add, delete or change lumen charges at a resolution equal to the multimericity of the pore. In the case of the heptameric aerolysin, when we mutate for instance a negative amino acid to a neutral one, the resulting assembly will have lost seven negative charges compared to the wild type (wt) pore. Aerolysin wt has 13 charged amino acid positions in the barrel region, thus corresponding to 13 rings of seven charged amino acids at given z-positions along the barrel (Figure 3a). Two of these rings have amino acids pointing outwards towards the electrolyte and membrane (K229 and E237), leaving 11 charged rings with amino acids pointing inside the pore lumen. The upper 4 charged positions come in clear pairs where a negative ring is right above or below a positive one

(R282 and D216; R220 and D222), and create the first known constriction of the pore[14,36]. The remaining 7 charged positions are located in the transmembrane region of the barrel: K238 and E258 are also right next to each other, followed by K242, E254, E252, K244 and K246 (Figure 3a), which form the second sensing constriction.

We mutated different combinations of these charged amino acids to change distribution of the pore lumen and thus measured a library of 26 different aerolysin mutants (S.Figure 3). In what follows, we first focus on the consequences of mutations over the open-pore ionic transport by using high frequency sweeps at low pore numbers. We then study the effect of mutations on the gating behaviour. We report in Figure 3b, *IV* curves measured with high frequency sweeps for all our aerolysin mutants (a version separated for distinguishability can be found in S.Figure 4). A first observation is that modifying lumen charges has dramatic consequences over the shape of the open-pore *IV* curve. Convex and concave rectification can be observed, as well as linear behaviour. Further, we find that the conductance of all mutants is below the bulk theoretical conductance of 2 nS by a factor of 2-8 (S.Table 1). We attribute the reduced and nonlinear ionic conduction to the presence of energy barriers arising from the combination of lumen charge and nanometric confinement. Altogether, these results show that ion transport through aerolysin is controlled by lumen charges and highly sensitive to its modifications which are easily achieved via well-established bio-engineering processes.

The effect of ionic rectification, also known as nanofluidic diode, has been the study of many experimental and theoretical studies mainly in solid-state nanofluidics[37–39]. However, these focused on relatively large channels (~10-100 nm in diameter) compared to ours, with spatially-extended surface charges and geometrical asymmetries. Here, we developed a theoretical framework to tackle the effect of individual, localised charge in a biological pore with sub-nanometric radius. To rationalise this, we derived an analytical theory (detailed in S.Section 3) accounting for rectification and linking its magnitude to the distribution of charge in the pore. Briefly, we modelled aerolysin as a cylindrical pore with a distribution of surface charges ρ corresponding to charged residues (Figure 3a). These charges define the potential energy landscape experienced by diffusing ions. When an electric field is applied, ions accumulate downstream of potential wells and upstream of potential barriers (Figure 3a & S.Figure 13). We observe an excellent agreement between the model and experimental data (Figure 3c). In particular, our model correctly predicts that the charged groups located near, but not at the mouth of the pore play a key role in ionic conduction.

When removing all above-mentioned charged amino acids present in aerolysin wt, the resulting *IV* curve is perfectly ohmic (S.Figure 4). We can thus deterministically control the degree of rectification as well as completely suppressing it, relying on the accurate mutation. We also experimentally confirmed that variations in ionic transport are mainly controlled by charge modification rather than a change in diameter by observing that mutating lysines (K) to alanine (A) (89 g/mol), serine (S) (105 g/mol) or the much larger glutamine (Q) (146 g/mol) is nearly equivalent (S.Figure 3). Having fully rationalised the relationship between lumen charge and open-pore ionic conduction, we now study the influence of lumen charges and their modification on the gating.

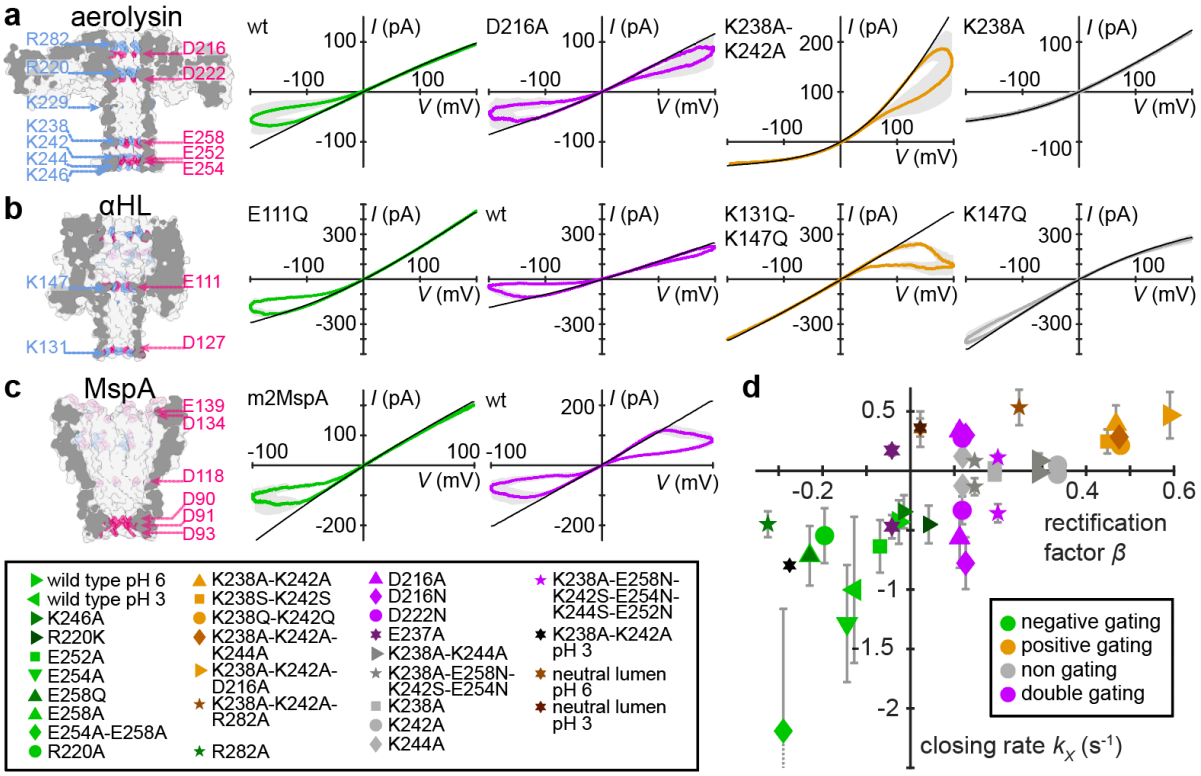

Figure 4 | Gating behaviour measured with different aerolysin (a), α-HL (b) and MspA (c) mutants, showcasing the great tunability of gating by changing lumen charge. Mutants gating at negative potentials displayed in green, at positive potentials in orange, mutants showing low levels of gating in grey and mutants that gate at both polarities in purple. Each plot displays the open-pore *IV* curve in black, displaying the differences in rectification. Further, each plot shows the standard deviation and number of experiments as a grey area and *n*. **d** Scatter plot of the pH response and all 26 aerolysin mutants' closing rates *versus* rectification factor *β*. Pores that show low gating or gating at both polarities are represented twice. For pores that show gating only in the negative or positive quadrant only one value is shown. The error bars show the standard deviation of closing rates of different repeat experiments. All experiments were conducted in 1 M KCl buffered to pH 6.2 with 10 mM phosphate. Sinusoidal forcing was applied at 0.1 Hz and 200 mV amplitude (100 mV for MspA wt and m2MspA).

Gating is dependent on the pore lumen charge.

We now examine the gating behaviour of our mutant library. We display in Figure 4a-c the *IV* curve obtained for several mutants of aerolysin, α-HL and MspA using low-frequency sinusoidal sweeps. We can observe that, depending on the mutations, gating can be observed at positive, negative or both polarities, or be largely absent. Gating further is additive i.e. two mutations (K238A, K242A) that individually lead to a suppression of the gating, collectively (K238A-K242A) lead to positive gating (opposite from aerolysin wt). Taken together with previous observations[3,25,40,41], this demonstrates both the universality of the phenomenon and its sensitivity to local charge variations. To further back the phenomenon's universality, we confirmed the previously observed increase in gating with decreasing charge carrier concentration[19,42] and pH[18,42–44] (S.Figure 9). As for the rectification, we verified that gating is dependent on the charge but not on the size or hydrophilicity of the exchanged amino acids. Indeed, the gating behaviours of K238A-K242A, K238S-K242S and K238Q-K242Q as well as D216A and D216N are highly similar (S.Figure 7, S.Table 1). Since A, S, Q and N are all non charged but differ in size and hydrophobicity, this leads us to conclude that the change of charge is the determining factor of gating. Gating, like rectification, is thus highly sensitive to the charge distribution in the pore lumen. Since both phenomena share a common dependency, we explore their correlation.

For aerolysin, we observed a correlation between closing rate, obtained from low frequency sweeps and rectification factor β, obtained from high frequency sweeps (Figure 4d). This means that the gating is most likely to occur at the polarity where the open-pore current is highest as can be observed in Figure 1c and Figure 4a. The correlation between the closing rate and β, which our rectification model previously showed to be solely dependent on lumen charge, clearly indicates the central role of lumen charge in the gating phenomenon.

Overall, we find that lumen charge effectively tunes gating in aerolysin, α-HL and MspA (Figure 4a-c). While gating is found to occur even in absence of any lumen charge (as illustrated by pores with neutral lumen S.Figure 7), the modification of charged residues can inhibit it or even invert its polarity dependence (Figure 4). This indicates that gating does not depend solely on lumen charge. Therefore we conclude that the gating is a combination of a charge-independent process and one dependent on lumen charges.

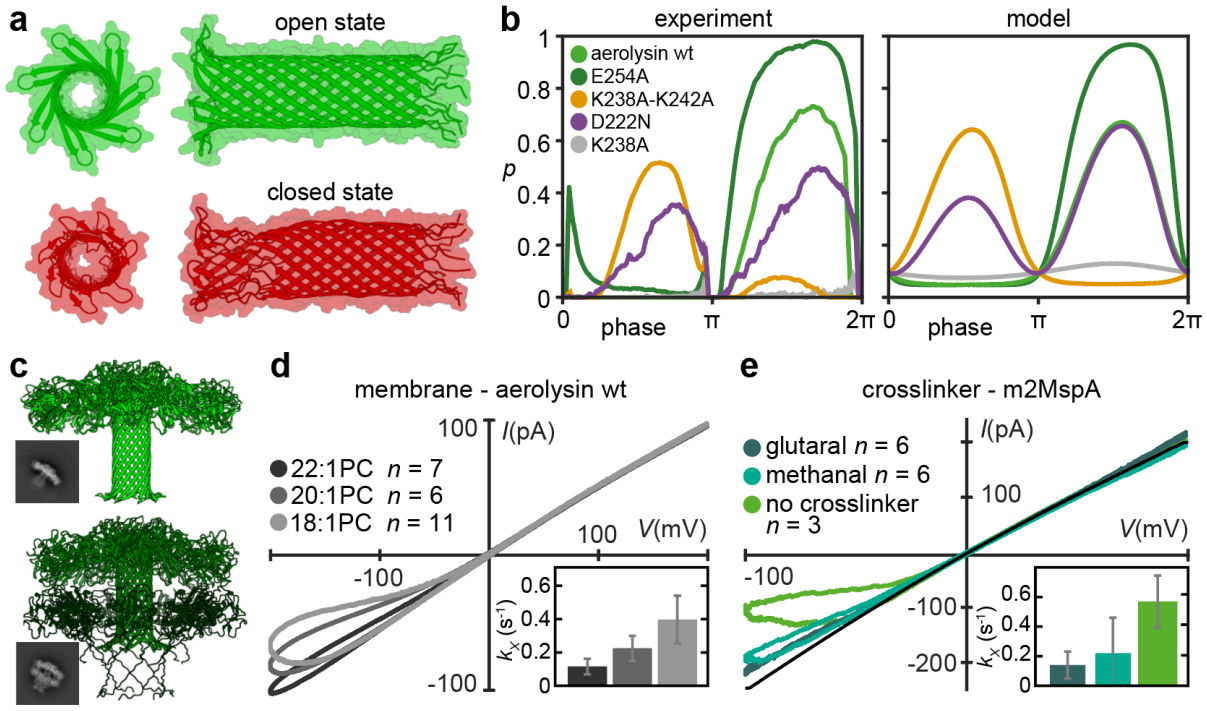

Figure 5 | Evidence in support of a structural deformation. a Sketch illustrating both states of the model. The increasing electrophoretic force acting on charged residues in the structure destabilise the β-barrel leading to a local decrease in channel diameter which reduces the ionic current. **b** Closed-state probability plotted against the phase of the voltage for aerolysin wt and four representative mutants obtained from experiments **(left)** and biophysical model **(right)** see S.Section 5 for details. The model accurately predicts if the given mutant is a positive, a negative or a double gater. It also predicts that the E254A mutant gates stronger than aerolysin wt. **c** Alignment of the refined structures of wt (light green) and the mutant (green) of a fully formed pore (top) and stack of a mutant pore (green) and a mutant pre-pore (dark green) (bottom). The latest is frequently observed only for the E254A-E258A mutant. Corresponding cryo-EM particles of the two populations are shown. **d** Gating behaviour of aerolysin wt for different membrane thickness (1 M KCl, 10 mM phosphate, pH 6.2, 0.1 Hz). Inset: extracted closing rate for the three probed membrane thicknesses. **e** Gating behaviour of m2MspA and m2MspA crosslinked with glutaral and methanal (1 M KCl, 10 mM phosphate, pH 6.2, 0.1 Hz). Inset: extracted closing rate for the pristine and crosslinked pores.

Gating is consistent with a conformational change

A reversible change of lumen conformation, triggered by voltage and controlled by surface charge as well as mechanical properties has been previously hypothesised for the studied pore-forming proteins[22] and was demonstrated for structurally different voltage-gated ion channels[10,45]. While obtaining direct experimental proof of a conformational change at these length scales is challenging, our dataset combines several clues pointing in that direction.

First, we develop an analytical biophysical model for the gating mechanism in aerolysin. Our model assumes that gating is induced by the partial unfolding of the β-barrel in the regions that are highly charged, in agreement with our mutant library (see S. Section 5 for extended discussion). The electric field exerting a force on the charged residues eventually overcomes the binding energy of the surrounding intermolecular forces which allows for an inward deformation of the barrel, yielding the conductance drop (Figure 5a). In Figure 5b, we observe good qualitative agreements between theory and experiments. Our model accounts for a number of key aspects of gating, like the existence of double gaters or of mutants that rectify but do not gate. In addition, the high variability of closed-state currents could be attributed to the disordered nature of these deformations (Figure 1d). This interpretation is also consistent with the evolution of gating with temperature, ionic strength and salt, as those parameters are known to control protein unfolding (S.Figure 9, S.Section 5).

We also perform several control experiments corroborating the hypothesis of voltage-induced structural deformations. When comparing cryo-EM structures of aerolysin wt and the strongly gating E254A-E258A mutant, we find that a significant amount of the E254A-E258A particles appear in dimeric pore stacks formed by one mature aerolysin pore within an aerolysin pre-pore (Figure 5c), similar to what previously found with a crosslinked K246C-E258C mutant. This indicates that, while aerolysin wt univocally forms a mature pore barrel in multiple membrane-mimicking environments[46], the E254A-E258A mutant shows a much lower efficiency for barrel formation as roughly half of the particles observed are trapped in the pre-pore conformation where the barrel is not yet formed.. This directly shows that mutations impact both the charge and the mechanical stability. Another hint is the dependency of the gating with membrane thickness (Figure 5d). Membrane thickness and composition is known to influence the dynamics of membrane proteins[47], and has been implicated in gating[48,49]. By changing the lipid tail length, we find that gating decreases with increasing membrane thickness. In the case of the biological nanopores in our study, the change in hydrophobic mismatch, pressure and tension changes, as well as the steric hindrance effects with the above-membrane parts of the protein are likely the influencing factors. The observation that gating is membrane-dependent points to the transmembrane region as the active site of the mechanism. To further verify the hypothesis of a conformational change, we crosslinked the highly-gating m2MspA pore with glutaral or methanal in order to increase its mechanical stability (Figure 5e). We find that such crosslinked pores do not gate while maintaining the same rectification and conductance (S.Table 2) as the untreated m2MspA.

The mechanical stability likely changes between mutants because mutating any charged residue in the pore lumen changes not only the charges but also the hydrogen bonding network, salt bridges, and other intermolecular forces which leads to the altered mechanical stability of the pore[18]. The intricate interplay between lumen charge and mechanical deformations within nanometric confinement explains the difficulty in characterising and understanding the phenomenon. The overwhelming uniformity with which these pores react to voltage, frequency, temperature, ionic strength, pH and lumen charge distribution indicates a common mechanism. As proposed previously[11], that deformation should be located in the transmembrane region which is common to all β-barrel forming toxins or pores. We reached a comprehensive understanding of this mechanism by relying on time-varying forcing as well as a wide library of mutants, cross-linked pores and membrane modification.

Conclusion and Outlook

β-barrel forming toxins or transporters have different functions in biology but all of them are transporting ions, water and small solutes. The regulation of molecular transport through such pores with voltage is a key feature of living organisms. We display successful rationalisation of biological ion-transport processes using a nanopore characterisation technique relying on alternative current. We show that the heterogeneous lumen charge controls two distincts nonlinearities: open-pore rectification and gating. Our work comprises a wide database elucidating this phenomenology beyond what has been shown in numerous previous studies[11,20,22]. We put forward that gating arises from a conformational change in the transmembrane region of the pore and our results lay down the groundwork for deeper characterizations of this phenomenon. The conformational dynamics of the lumen we uncovered here could be confirmed using techniques such as single-molecule FRET, and our theoretical developments could be supplemented with coarse-grained approaches to simulate the pore dynamics. Furthermore, our method could be extended to the numerous different biological nanopores in order to deepen our understanding of Nature's sophisticated ionic machinery.

Understanding nanopore physics is irremissible to tap into their full power, both for emerging techniques like protein sequencing as well as computing applications with diverging strategies. On the one hand, designing gating-free mutants as well as de-novo designed nanopores[50] tailored for sensing applications will remove limitations for this research field

and nascent industry. On the other hand, rectification and gating can be employed to generate iontronic components like resistors, diodes or memristors with a tuning resolution down to 7 single charges. While the construction of multi-component ionic computing systems is still at its infancy[33], our results show that such networks could potentially use biological building blocks with dimensions similar to those of state-of-the-art electronic transistors.

Acknowledgements

We are grateful to Dr. Michael Mayer and Dr. Gisou Van Der Goot for their insightful discussions and thoughtful feedback. We acknowledge funding from the European Research Council (grants 101020445—2D-LIQUID N.R. and A.R.MSCA No. 101034413 P.R.), the Swiss National Science Foundation (grants 205321_192371, and 200021L_212128 to M.D.P., TMPFP2-217134 to T.E, and IZSEZ0_183779 to J. H. G. and A. R.) and the Swiss National Supercomputing Centre (CSCS) for access to the HPC resources used to run MD simulations.

Author contributions

S.F. Mayer, T. Emmerich, N. Ronceray, M. Dal Peraro and A. Radenovic conceived and designed the project. S.F. Mayer and M.F. Mitsioni have conducted and analysed planar lipid bilayer experiments. S. Soussou, J. Jeanneret-Grosjean, L. Van Den Heuve,l and A. Fulciniti have conducted some of the planar lipid bilayer experiments. L. Van Den Heuvel has written the data processing code and processed the simulation data under the supervision of S.F. Mayer. P. Robin has built the models for rectification and gating. L.A. Abriata has run the simulations and helped with their processing. L.F. Krapp has analysed the single pore aerolysin gating data and simulation data. M.F. Mitsioni, with the help of S. Vacle, L. Feletti and A. Möller, produced nanopores under the supervision of M.J. Marcaida. J.S. Anton has done all cryo-EM work and conducted the blood assay. H.D. Brinkerhoff, A.H. Laszlo and J.H. Gundlach provided initial guidance setting up DC measurements and provided feedback on the project. S.F Mayer, M.F. Mitsioni, N. Ronceray, and T. Emmerich wrote the manuscript. with the input from all authors. A. Radenovic and M. Dal Peraro jointly supervised this work.

Competing interests

The authors declare that they have no conflict of interest.

Materials and Methods

M&M Section 1. Material

We purchased 1,2-diphytanoyl-sn-glycero-3-phosphocholine (DPhPC), 1,2-di-O-phytanyl-sn-glycero-3-phosphocholine (DoPhPC), 1,2-dimyristoleoyl-sn-glycero-3-phosphocholine ($14{:}1_{\Delta 9\text{-Cis}}$PC), 1,2-dipalmitoleoyl-sn-glycero-3-phosphocholine ($16{:}1_{\Delta 9\text{-Cis}}$PC), 1,2-dioleoyl-sn-glycero-3-phosphocholine ($18{:}1_{\Delta 9\text{-Cis}}$PC), 1,2-dieicosenoyl-sn-glycero-3-phosphocholine ($20{:}1_{cis}$PC), 1,2-dierucoyl-sn-glycero-3-phosphocholine ($22{:}1_{cis}$PC) dissolved in chloroform from Avanti Polar Lipids (Birmingham, AL, USA), Plasmids from Genscript (Piscataway, NJ, USA), Turbonuclease from Lucerna-Chem AG (Luzern, CH), HEPES from Chemie Brunschwig AG (Basel, CH), 0.45 µm Rotilabo PVDF syringe filter from Carl Roth GmbH & Co. KG (Karlsruhe, DE), isopropyl β-d-1-thiogalactopyranoside (IPTG) from Huberlab (Aesch, CH), defibrinated sheep blood from Rockland Immunochemicals, Inc. (Limerick, PA, USA), HiPrep 26/10 Desalting column and HisTrap HP column from Cytiva (Marlborough, MA, USA), and all other chemicals from Merck (Darmstadt, DE). All electrolyte solutions used in bilayer experiments were buffered with 10 mM phosphate and filtered through 0.22 µm pore size PES vacuum filters from VWR International (Radnor, PA, USA). We used purified water (18.2 MΩ) from a milli-Q water purifying system. Ag/AgCl wire electrodes were made by immersing one side of high purity silver wire pieces in bleach for 1 h and subsequent washing with water. Lipids were aliquoted at 0.2 mg per glass vial, chloroform was evaporated under vacuum and vials subsequently closed with Polytetrafluoroethylene (PTFE) lined caps, in an argon glove box and stored at -20 °C to avoid oxidation. Lipids were dissolved freshly in octane or pentane at 10 mg/mL.

Aerolysin purification

The clone of the full-length aerolysin wt protein (in the pET22b vector with a C-terminal hexa-histidine-tag (His-tag)) was kindly provided by the Van der Goot laboratory at EPFL. The mutants were generated by Genscript using the wt plasmid as a template. The aerolysin protein was produced as previously described by Cao et al.[14]. In brief, plasmids were transformed into BL21 (DE3 Plys) *E. coli* cells by heat shock. Cells were grown to an optical density of 0.6 to 0.7 at 600 nm in LB media. Protein expression was induced by the addition of 1 mM IPTG and subsequent growth overnight at 18 °C. Cell pellets were resuspended in lysis buffer (500 mM NaCl, 50 mM tris, pH 7,4), mixed with cOmplete Protease Inhibitor Cocktail, and then lysed by sonication on ice. Turbonuclease solution was added to the resulting suspension which was then centrifuged (20'000 *g* for 30 minutes at 4 °C). After syringe filtration over a 0.45 µm filter, the supernatant was applied to a HisTrap HP column previously equilibrated with lysis buffer. The protein was eluted as a monomer with a gradient of 30 column volumes of elution buffer (500 mM NaCl, 50 mM tris, 500 mM imidazole, pH 7,4). aerolysin-containing fractions were then buffer-exchanged to aerolysin-final-buffer (20 mM tris, 150 mM NaCl, pH 7.4) using a HiPrep Desalting column. The purification of the selected fractions was confirmed by SDS-polyacrylamide gel electrophoresis. Aerolysin was concentrated to 0.5 mg/mL and stored at -20 °C. The

activation of aerolysin to undergo conformational changes and enable heptamerization is achieved by incubating it with trypsin in agarose at a ratio of 1:4 (trypsin:pore, *v/v*).

α-HL purification

The coding sequences for all α-HL mutants were custom synthesised, optimised for *E. coli* expression and inserted into the pET28-b vector between the NcoI and XhoI cleavage sites, such that the resulting proteins carry a C-terminal His-tag for later purification. Plasmids were transformed in BL21 (DE3) cells by heat shock transformation. The cells were grown in LB medium at 37 °C until optical density of 0.6 to 0.7 at 600 nm at which point protein expression was induced by the addition of 0.1 mM IPTG, followed by subsequent overnight growth at 18 °C. Cell pellets were resuspended in lysis buffer (500 mM NaCl, 20 mM HEPES, 1% Triton X-100 (*v/v)*, pH 8.0), mixed with cOmplete Protease Inhibitor Cocktail, and then lysed by using sonication on ice. Turbonuclease solution was added to the resulting suspension which was then centrifuged (20'000 *g* for 60 minutes at 4 °C). After syringe filtration over a 0.45 µm filter, the supernatant was applied to a HisTrap HP column previously equilibrated with lysis buffer. The column was then washed with 3 column volumes of lysis buffer followed by a wash with 10 column volumes of buffer A (500 mM NaCl, 20 mM HEPES, 5 mM imidazole, pH 8.0). The α-HL heptamers were then eluted with a linear gradient of buffer B (500 mM NaCl, 20 mM HEPES, 500 mM imidazole, pH 8.0). Peak fractions were analysed by SDS-polyacrylamide gel electrophoresis and only the fractions with the α-HL heptamer were retained for subsequent planar lipid bilayer experiments.

MspA purification

The coding sequences for all MspA mutants was custom synthesised, optimised for *E. coli* expression and inserted into the pET28b vector, between the NcoI and XhoI cleavage sites, such that the resulting proteins have a C-terminal His-tag to aid purification. Plasmids were transformed in *E. coli* BL21 (DE3) cells. Protein expression was induced by the addition of 0.1 mM IPTG as soon as the cells reached an optical density of 0.6 and subsequent growth overnight at 18 °C. Cell pellets were resuspended in lysis buffer (100 mM sodium phosphate, 0.1 mM EDTA, 150 mM NaCl, 0.5% (*w/v*) Genapol X-80, pH 6.5), mixed with cOmplete Protease Inhibitor Cocktail, and then lysed using sonication on ice, followed by boiling at 60 °C for 10 minutes. Turbonuclease solution was added to the resulting suspension which was then chilled in ice for 10 minutes. To remove intact cells and cell debris, the samples were centrifuged at 20'000 *g* for 60 minutes at 4 °C. After syringe filtration over a 0.45 µm filter, the supernatant was applied to a HisTrap HP column previously equilibrated with lysis buffer. The column was then washed with 3 column volumes of lysis buffer, followed by 10 column volumes of buffer C (500 mM NaCl, 20 mM HEPES, 5 mM imidazole, 0.5% (*w/v*) Genapol X-80, pH 8.0). The MspA octamers were then eluted with a linear gradient of buffer D (500 mM imidazole, 500 mM NaCl, 20 mM HEPES, 0.5% (*w/v*) Genapol X-80, pH 8.0). Peak fractions were analysed by SDS-polyacrylamide gel electrophoresis and only the fractions with the MspA octamer were retained for subsequent planar lipid bilayer experiments.

The crosslinked pores were prepared as follows. 100 µL of MspA wt or m2MspA were mixed with 10 µL of 8% *v/v* glutaral in water to a final concentration of 0.8% glutaral and incubated for 10 minutes before being added to the experiments. For pores crosslinked with methanal,

100 µL of pore solution were mixed with 5 µL of 20% *v/v* methanal in water to a final concentration of 1% *v/v* methanal and incubated for 10 minutes before addition to the experiment.

M&M Section 2. Experiments

Planar lipid bilayer experiments

Unless stated otherwise, an Orbit Mini (Nanion Technologies, Munich, DE) with 50 µm aperture MECA-4 chips (Ionera Technologies GmbH, Freiburg, DE) was used for all experiments. Bilayers were painted by dipping, pipette tips in 10 mg/mL DPhPC in octane, and subsequent dabbing on Kimwipes, so that all visible liquid was removed from the pipette tip. The pipette tip was then immersed in the electrolyte solution filled MECA-4 chip, placed over one of the four apertures and a bubble was pushed in and out of the pipette tip until a membrane was formed. This usually required several tries, exchanging lipid-primed pipette tips frequently. For all open-pore *IV* curve recordings, we pretreated PTFE films (Eastern Scientific LLC, Rockville, MD, USA) with a single aperture with a diameter of 50 µm by pipetting 1 µL of 1% (*v/v*) hexadecane in hexane onto both sides of the aperture of the PTFE film. We mounted the PTFE film in a PTFE chamber using high-vacuum grease (Dow Corning Corporation, Midland, MI, USA). The PTFE film separated two compartments containing aqueous electrolyte, which were only connected by the aperture in the PTFE film over which the bilayer was formed. We formed planar lipid bilayers across the aperture using a technique previously described[26,51]. Briefly, we added electrolyte solution to both compartments so that the level was below the aperture and pipetted 3 µL of DPhPC dissolved in pentane onto the surface of the electrolyte solution. After the pentane evaporated, a lipid monolayer formed at the air-aqueous interface. We raised and lowered the electrolyte solution until we measured a very small baseline current (-3 pA < I < 3 pA) indicating that a membrane had formed. All single pore DC experiments and the experiments with sine wave frequencies at and below 0.001 Hz were measured in painted bilayers formed on selfmade PTFE/FEP supports made from Dual-Shrink tube (Zeus, Orangeburg, SC, USA) using a tungsten needle, sharpened from a welding electrode. Supports were pretreated by pipetting 1 µL DoPhPC in hexane (2 mg/mL) onto the support, blowing through the support from the backside with an air filled syringe to clear it from the lipid solution. This pretreatment was repeated 2 times with short drying cycles in a desiccator under vacuum. The bilayer was painted from pure DoPhPC wetted with hexadecane with a two-haired fine paintbrush. We verified the stability (absence of leak currents; expected noise & capacitance level) of all bilayers by briefly applying transmembrane voltages of up to 200 mV. The current was measured with an axopatch 500B amplifier (Molecular Devices, LLC.,San Jose, CA, USA) through Ag/AgCl pellet electrodes (World Precision Instruments Inc., Sarasota, FL, USA) or Ag/AgCl wire electrodes. Ag/AgCl wire electrodes were chlorinated by immersing coiled silver wire in bleach for 1 h before rinsing thoroughly with demineralized water. After use electrodes were stripped from silver chloride with ammonium hydroxide and re-chlorinated. We assembled experimental setups inside Faraday cages. Voltages were applied externally through NI PXI-8336 & PXI-4461 controlled by in-house labview software, both applied voltage and resulting current were measured. We carried out all experiments at room temperature (23 to 25 °C) and tested all setups with different model cells to confirm

proper functionality of the amplifiers. We cleaned the setups by rinsing all parts that came in contact with the electrolyte, nanopores and lipids with several cycles of demineralized water and isopropyl alcohol. We subjected PTFE cells and films to additional cleaning with chloroform to remove vacuum grease.

Red blood cell assay

Defibrinated sheep blood was diluted in aerolysin-final-buffer until the optical density (OD) of the sample reached 1. For each mL of blood, 1 µL of trypsin in agarose was added. The concentration of aerolysin wt and aerolysin mutants was determined by measuring the absorbance at 280 nm with a microvolume UV-Vis spectrophotometer, and all mutants were diluted to a concentration of 5 mM in aerolysin-final-buffer. The blood sample was combined with the pores in a 96-well plate with transparent bottom to a final sample volume of 100 µL per well with a final pore concentration of 0.5 µM or 1 µM. The samples were gently mixed using a pipette. Triplicates were prepared for each pore and pore concentration. Additionally, three control samples containing only blood and trypsin were included as controls. The OD of each sample was monitored over a period of 1 hour, with OD measurements taken every 15 seconds. To compare the activity of each mutant, the measurements were normalised by dividing by the initial absorbance value of each sample. The absorbance was then plotted over time to visualise the lysis activity.

Cryo-EM

The aerolysin E254A-E258A sample in SMALP and cryo-EM grids were prepared as described previously[46]. The dataset was collected at the Dubochet Center for Imaging (Lausanne, CH) using the 300 kV TFS Titan Krios G4 equipped with a Cold-FEG and Falcon 4 detection. The dataset was collected in electron-counting mode (EER). The Falcon IV gain references were measured before starting the data collection. The data collection was performed using the TFS EPU software packages. Movies were recorded at a nominal magnification of 120,000x, corresponding to 0.658 Å/pixel with defocus values ranging from 0.8 to 1.7. The exposure dose was set to 50 e/Å^2. The datasets were processed in CryoSPARC[52]. The reported resolutions are based on the gold-standard Fourier shell correlation (FSC)=0.143 criteria[53] and local-resolution variations were estimated using CryoSPARC. For the model building the structure of aerolysin wt 9FM6 and the pre-pore mutant 5JZT were as used as an initial model which was fit into the cryo-EM map using Phenix[54] and were manually adjusted using Coot[55] and relaxed refinement in Rosetta[56] and Phenix. In the E254A-E258A pore structure the residues 14-23 and 246-251 and in the post-prepore structure the residues 197-308 were not built due to a lack of density in these areas.

M&M Section 3. Simulations

The systems for atomistic MD simulations were prepared with the CHARMM-GUI[57] website, using the structure of heptameric aerolysin wt available in the PDB with ID 5JZT, onto which the desired mutations were crafted using PyMOL. The protein heptamers were placed in the DPhPC membranes (CHARMM's lipid name PHPC) using PPM 2.0 through the

CHARM-GUI interface. The systems were further prepared (solvated and neutralised) with standard CHARMM-GUI procedures and parameters, in 1 M KCl. The systems were parametrized in CHARMM-GUI using CHARMM36m[58] for the protein components and the corresponding version of TIP3P water, plus the standard CHARMM parameters available for DPhPC lipids. After standard CHARMM-GUI-provided minimization and equilibration procedures with standard parameters and restrain strengths using Gromacs 2022, we ran the production simulations applying the indicated voltages using the same MD engines and standard production files from CHARMM-GUI (i.e. semi-isotropic pressure coupling to 1 atm, a temperature of 298 K, 2 fs integration steps, LINCS-based restraints on hydrogens, and PME electrostatics with 12 Å cutoff) but applying restraints on the Cα atoms. These restraints allowed sampling the effect of sidechain-contributed electrostatics on ion currents without interference from structural perturbations that might be unrealistic given the limited resolution of the starting PDB structure and the high applied voltages.

Simulations were extended for around 400 ns; and for all subsequent analysis only the last 280 ns of the production phase were used. These analyses were carried out using standard VMD commands and custom scripts as detailed below.

The electrostatic potential was extracted from whole-atom simulations using the PME Electrostatics plugin[59] in VMD[60]. The potential of the box was calculated for every tenth frame, from which a time-average was calculated. To compute an average potential inside the pore channel along the z-axis, the box was divided in 200 subvolumes in the z-direction. In each subvolume, the pore channel diameter was defined as 90% of the diameter of the smallest enclosing circle of all water atoms in that subvolume, throughout all timeframes in the simulation. The reported potential value at a specific z-height is an average of the pore channel in the subvolume corresponding to that height.

The ionic flux at a given voltage bias was extracted from whole-atom simulations using a previously published method[59]. In brief, the instantaneous ionic current at time *t* was

$$I(t) = \frac{1}{\Delta t\, L_p} \sum_{ion=1}^{N_{ion}} Q_{ion} \cdot [z_{ion}(t + \Delta t] - z_{ion}(t)] \,, \qquad \text{Equation 3}$$

Where Δt = 0.2 ns is the time gap between consecutive pairs of simulation snapshots written during production, L_p is the length of the pore barrel (9 nm for aerolysin), N_{ion} is the number of ions inside the pore lumen and Q_{ion} and z_{ion} are the charge and z-coordinate of ion, respectively. The average current at a given voltage bias was computed by applying a linear regression to the cumulative sum of $I(t)$.

M&M Section 4. Data Analysis

Two-state description:

We simplified the gating process of nanopores as a stochastic switching between two discrete conductance levels, the open-pore state $G_O(V)$, and the closed-pore state $G_x(V)$. In accordance with the gating measurements on single pores (Figure 1), we set $G_x(V) = \epsilon \cdot$

$G_O(V)$ with ϵ = 0.14 which is the average gating level of 4 different recorded pores. In this simplified 2-state system, the probability of a pore to be closed, $p(t)$, is governed by Equation 2. To experimentally measure the mean voltage-dependent opening and closing rates, k_O and k_X, we applied a step-current with bias voltage $V(t) = V_{app.}$ to an ensemble of pores. The fraction of open-pores then decays exponentially as

$(1 - p(t)) = 1 + p_{equilib}(e^{-t/\tau} - 1)$, where Equation 4

$p_{equilib} = \frac{k_X(V_{app.})}{k_O(V_{app.})+k_X(V_{app.})}$, and

$\tau = \frac{1}{k_O(V_{app.})+k_X(V_{app.})}$.

Thus, by applying voltage steps of various bias voltages to a pore ensemble and extracting $p_{equilib}$ and τ from the measured current response, the opening and closing rates were estimated. Exponential fitting was implemented as a weighted linear regression of

$t =- \tau\cdot[log(|p_{equilib} - p(t)|) - log(p_{equilib})]$, Equation 5

where the optimal τ and $p_{equilib}$ were those that minimised the weighted residual sum of squares. The weights decayed logarithmically from 1 (at t = 0) to 10^{-15} (at $t = t_{end}$ = 35 s) to ensure a good estimation of τ.

At low bias voltages ($V_{app.}$ < 60 mV), where the closing rate is almost zero so that an accurate estimation of τ becomes problematic, pores were first closed by applying a high bias voltage of 200 mV for 35 seconds, after which the voltage was reduced to $V_{app.}$ and the opening rate was estimated as $k_O(V_{app.}) = \tau^{-1}$.

Alternating voltage traces:

In the general case, assuming only 2 conductance states, the expected value for the conductance of an ensemble of gating pores $G(t)$ is given by Equation 1. Given the 2-state assumption $G_x(V) = \epsilon \cdot G_O(V)$, the expected ensemble current, $I(t)$, is

$\frac{I(t)}{I_O(t)} = \frac{G(t)}{N_p\cdot G_0(t)} = 1 - p(t) \cdot (1 - \epsilon)$, Equation 6

where $I_O(t) = N_p\cdot G_O(t)\cdot V(t)$ is the open-pore current obtained from AC measurements at high frequency. Thus, from a recording of the ensemble current response to an alternating voltage, the frequency-dependent closed-pore probability could be estimated as

$p(t) = \frac{1}{1-\epsilon} \cdot (1 - \frac{I_{ens}(t)}{I_O(t)})$, Equation 7

Where $I_{ens}(t)$ is the average measured ensemble current of multiple AC cycles in the same ensemble. Note that for each cycle, the ensemble current was normalised by the estimated

number of pores in that cycle, N_p. To find the number of pores, a voltage window where no gating took place was predefined, and the current in this window was fitted to the *IV* curve in the same window using a linear regression, the slope of which gave N_p. Throughout a cycle, the closing rate k_X in Hz was estimated as the maximum of $\frac{dp(t)}{dt}$.

References

1. Margheritis, E., Kappelhoff, S. & Cosentino, K. Pore-Forming Proteins: From Pore Assembly to Structure by Quantitative Single-Molecule Imaging. *Int. J. Mol. Sci.* **24**, 4528 (2023).
2. Capone, R., Blake, S., Rincon Restrepo, M., Yang, J. & Mayer, M. Designing Nanosensors Based on Charged Derivatives of Gramicidin A. *J. Am. Chem. Soc.* **129**, 9737–9745 (2007).
3. Butler, T. Z., Pavlenok, M., Derrington, I. M., Niederweis, M. & Gundlach, J. H. Single-molecule DNA detection with an engineered MspA protein nanopore. *Proc. Natl. Acad. Sci.* **105**, 20647–20652 (2008).
4. Derrington, I. M. *et al.* Nanopore DNA sequencing with MspA. *Proc. Natl. Acad. Sci.* **107**, 16060–16065 (2010).
5. Manrao, E. A. *et al.* Reading DNA at single-nucleotide resolution with a mutant MspA nanopore and phi29 DNA polymerase. *Nat. Biotechnol.* **30**, 349–353 (2012).
6. Deamer, D., Akeson, M. & Branton, D. Three decades of nanopore sequencing. *Nat. Biotechnol.* **34**, 518–524 (2016).
7. Brinkerhoff, H., Kang, A. S. W., Liu, J., Aksimentiev, A. & Dekker, C. Multiple rereads of single proteins at single–amino acid resolution using nanopores. *Science* **374**, 1509–1513 (2021).
8. Wang, Y., Zhao, Y., Bollas, A., Wang, Y. & Au, K. F. Nanopore sequencing technology, bioinformatics and applications. *Nat. Biotechnol.* **39**, 1348–1365 (2021).
9. Mayer, S. F., Cao, C. & Dal Peraro, M. Biological nanopores for single-molecule sensing. *iScience* **25**, 104145 (2022).
10. Bertil Hille. *Ion Channels of Excitable Membranes*. (Sinauer Associates, Inc. Publishers, Sunderland, Massachusetts USA, 2001).
11. Bainbridge, G., Gokce, I. & Lakey, J. H. Voltage gating is a fundamental feature of porin and toxin β-barrel membrane channels. *FEBS Lett.* **431**, 305–308 (1998).
12. Dessaux, D., Mathé, J., Ramirez, R. & Basdevant, N. Current Rectification and Ionic Selectivity of α-Hemolysin: Coarse-Grained Molecular Dynamics Simulations. *J. Phys. Chem. B* **126**, 4189–4199 (2022).
13. Miedema, H. *et al.* A Biological Porin Engineered into a Molecular, Nanofluidic Diode. *Nano Lett.* **7**, 2886–2891 (2007).
14. Cao, C. *et al.* Single-molecule sensing of peptides and nucleic acids by engineered aerolysin nanopores. *Nat. Commun.* **10**, 4918 (2019).
15. Mueller, P. & Rudin, D. O. Induced excitability in reconstituted cell membrane structure. *J. Theor. Biol.* **4**, 268–280 (1963).
16. Schindler, H. & Rosenbusch, J. P. Matrix protein from Escherichia coli outer membranes forms voltage-controlled channels in lipid bilayers. *Proc. Natl. Acad. Sci. U.*

S. A. **75**, 3751–3755 (1978).
17. Menestrina, G. Ionic channels formed byStaphylococcus aureus alpha-toxin: Voltage-dependent inhibition by divalent and trivalent cations. *J. Membr. Biol.* **90**, 177–190 (1986).
18. Kasianowicz, J. J. & Bezrukov, S. M. Protonation dynamics of the alpha-toxin ion channel from spectral analysis of pH-dependent current fluctuations. *Biophys. J.* **69**, 94–105 (1995).
19. Mohammad, M. M. & Movileanu, L. Impact of Distant Charge Reversals within a Robust β-Barrel Protein Pore. *J. Phys. Chem. B* **114**, 8750–8759 (2010).
20. Nestorovich, E. M. & Bezrukov, S. M. Beta-Barrel Channel Response to High Electric Fields: Functional Gating or Reversible Denaturation? *Int. J. Mol. Sci.* **24**, 16655 (2023).
21. Paulo, G. *et al.* Hydrophobically gated memristive nanopores for neuromorphic applications. *Nat. Commun.* **14**, 8390 (2023).
22. Mayse, L. A. & Movileanu, L. Gating of β-Barrel Protein Pores, Porins, and Channels: An Old Problem with New Facets. *Int. J. Mol. Sci.* **24**, 12095 (2023).
23. Colombini, M. Voltage gating in the mitochondrial channel, VDAC. *J. Membr. Biol.* **111**, 103–111 (1989).
24. Bocquet, L. & Charlaix, E. Nanofluidics, from bulk to interfaces. *Chem. Soc. Rev.* **39**, 1073–1095 (2010).
25. Maglia, G., Restrepo, M. R., Mikhailova, E. & Bayley, H. Enhanced translocation of single DNA molecules through α-hemolysin nanopores by manipulation of internal charge. *Proc. Natl. Acad. Sci.* **105**, 19720–19725 (2008).
26. Hanke, W. & Schlue, W.-R. *Planar Lipid Bilayers Methods and Applications*. (Academic Press, 1993).
27. Bayley, H. & Martin, C. R. Resistive-Pulse SensingFrom Microbes to Molecules. *Chem. Rev.* **100**, 2575–2594 (2000).
28. Strukov, D. B., Snider, G. S., Stewart, D. R. & Williams, R. S. The missing memristor found. *Nature* **453**, 80–83 (2008).
29. Sung, C., Hwang, H. & Yoo, I. K. Perspective: A review on memristive hardware for neuromorphic computation. *J. Appl. Phys.* **124**, 151903 (2018).
30. Kumar, S., Wang, X., Strachan, J. P., Yang, Y. & Lu, W. D. Dynamical memristors for higher-complexity neuromorphic computing. *Nat. Rev. Mater.* **7**, 575–591 (2022).
31. Robin, P. *et al.* Long-term memory and synapse-like dynamics in two-dimensional nanofluidic channels. *Science* **379**, 161–167 (2023).
32. Xiong, T. *et al.* Neuromorphic functions with a polyelectrolyte-confined fluidic memristor. *Science* **379**, 156–161 (2023).
33. Emmerich, T. *et al.* Nanofluidic logic with mechano-ionic memristive switches. *Nat. Electron.* 1–8 (2024) doi:10.1038/s41928-024-01137-9.
34. Emmerich, T. *et al.* Nanofluidics. *Nat. Rev. Methods Primer* **4**, 1–18 (2024).
35. Schindler, H. & Rosenbusch, J. P. Matrix protein in planar membranes: clusters of channels in a native environment and their functional reassembly. *Proc. Natl. Acad. Sci. U. S. A.* **78**, 2302–2306 (1981).
36. Cao, C. *et al.* Mapping the sensing spots of aerolysin for single oligonucleotides analysis. *Nat. Commun.* **9**, 2823 (2018).
37. Vlassiouk, I. & Siwy, Z. S. Nanofluidic Diode. *Nano Lett.* **7**, 552–556 (2007).

38. Karnik, R., Duan, C., Castelino, K., Daiguji, H. & Majumdar, A. Rectification of Ionic Current in a Nanofluidic Diode. *Nano Lett.* **7**, 547–551 (2007).
39. Poggioli, A. R., Siria, A. & Bocquet, L. Beyond the Tradeoff: Dynamic Selectivity in Ionic Transport and Current Rectification. *J. Phys. Chem. B* **123**, 1171–1185 (2019).
40. Liu, N., Samartzidou, H., Lee, K. W., Briggs, J. M. & Delcour, A. H. Effects of pore mutations and permeant ion concentration on the spontaneous gating activity of OmpC porin. *Protein Eng. Des. Sel.* **13**, 491–500 (2000).
41. Delcour, A. H., Adler, J. & Kung, C. A single amino acid substitution alters conductance and gating of OmpC porin ofEscherichia coli. *J. Membr. Biol.* **119**, 267–275 (1991).
42. Fologea, D. *et al.* Controlled Gating of Lysenin Pores. *Biophys. Chem.* **146**, 25–29 (2010).
43. Krasilnikov, O. V., Muratkhodjaev, J. N. & Zitzer, A. O. The mode of action of *Vibrio cholerae* cytolysin. The influences on both erythrocytes and planar lipid bilayers. *Biochim. Biophys. Acta BBA - Biomembr.* **1111**, 7–16 (1992).
44. Duret, G., Simonet, V. & Delcour, A. H. Modulation of Vibrio cholerae Porin Function by Acidic pH. *Channels* **1**, 70–79 (2007).
45. Aidley, D. J. & Stanfield, P. R. *Ion Channels: Molecules in Action*. (Cambridge University Press, 1996).
46. Anton, J. S. *et al.* Aerolysin nanopore structure revealed at high resolution in lipid environment. 2024.08.12.607338 Preprint at https://doi.org/10.1101/2024.08.12.607338 (2024).
47. Andersen, O. S. & Koeppe, R. E. Bilayer Thickness and Membrane Protein Function: An Energetic Perspective. *Annu. Rev. Biophys. Biomol. Struct.* **36**, 107–130 (2007).
48. Wiese, A. *et al.* Influence of the lipid matrix on incorporation and function of LPS-free porin from *Paracoccus denitrificans*. *Biochim. Biophys. Acta BBA - Biomembr.* **1190**, 231–242 (1994).
49. Lakey, J. H. & Pattus, F. The voltage-dependent activity of Escherichia coli porins in different planar bilayer reconstitutions. *Eur. J. Biochem.* **186**, 303–308 (1989).
50. Berhanu, S. *et al.* Sculpting conducting nanopore size and shape through de novo protein design. *Science* **385**, 282–288 (2024).
51. Montal, M. & Mueller, P. Formation of Bimolecular Membranes from Lipid Monolayers and a Study of Their Electrical Properties. *Proc. Natl. Acad. Sci.* **69**, 3561–3566 (1972).
52. Punjani, A., Rubinstein, J. L., Fleet, D. J. & Brubaker, M. A. cryoSPARC: algorithms for rapid unsupervised cryo-EM structure determination. *Nat. Methods* **14**, 290–296 (2017).
53. Scheres, S. H. W. & Chen, S. Prevention of overfitting in cryo-EM structure determination. *Nat. Methods* **9**, 853–854 (2012).
54. Liebschner, D. *et al.* Macromolecular structure determination using X-rays, neutrons and electrons: recent developments in Phenix. *Acta Crystallogr. Sect. Struct. Biol.* **75**, 861–877 (2019).
55. Emsley, P., Lohkamp, B., Scott, W. G. & Cowtan, K. Features and development of Coot. *Acta Crystallogr. D Biol. Crystallogr.* **66**, 486–501 (2010).
56. Wang, R. Y.-R. *et al.* Automated structure refinement of macromolecular assemblies from cryo-EM maps using Rosetta. *eLife* **5**, e17219 (2016).

57. Lee, J. *et al.* CHARMM-GUI Input Generator for NAMD, GROMACS, AMBER, OpenMM, and CHARMM/OpenMM Simulations Using the CHARMM36 Additive Force Field. *J. Chem. Theory Comput.* **12**, 405–413 (2016).
58. Huang, J. & MacKerell, A. D. CHARMM36 all-atom additive protein force field: validation based on comparison to NMR data. *J. Comput. Chem.* **34**, 2135–2145 (2013).
59. Aksimentiev, A. & Schulten, K. Imaging *α*-Hemolysin with Molecular Dynamics: Ionic Conductance, Osmotic Permeability, and the Electrostatic Potential Map. *Biophys. J.* **88**, 3745–3761 (2005).
60. Humphrey, W., Dalke, A. & Schulten, K. VMD: Visual molecular dynamics. *J. Mol. Graph.* **14**, 33–38 (1996).
61. Laszlo, A. H., Derrington, I. M. & Gundlach, J. H. MspA nanopore as a single-molecule tool: From sequencing to SPRNT. *Methods* **105**, 75–89 (2016).
62. Nestorovich, E. M. & Bezrukov, S. M. Beta-Barrel Channel Response to High Electric Fields: Functional Gating or Reversible Denaturation? *Int. J. Mol. Sci.* **24**, 16655 (2023).
63. Wilmsen, H. U., Pattus, F. & Buckley, J. T. Aerolysin, a hemolysin fromAeromonas hydrophila, forms voltage-gated channels in planar lipid bilayers. *J. Membr. Biol.* **115**, 71–81 (1990).
64. Wurl, A. *et al.* Filling the Gap with Long n-Alkanes: Incorporation of C20 and C30 into Phospholipid Membranes. *Langmuir* **38**, 8595–8606 (2022).
65. Zoni, V., Campomanes, P. & Vanni, S. Investigating the structural properties of hydrophobic solvent-rich lipid bilayers. *Soft Matter* **17**, 5329–5335 (2021).
66. Iacovache, I. *et al.* Cryo-EM structure of aerolysin variants reveals a novel protein fold and the pore-formation process. *Nat. Commun.* **7**, 12062 (2016).
67. Degiacomi, M. T. *et al.* Molecular assembly of the aerolysin pore reveals a swirling membrane-insertion mechanism. *Nat. Chem. Biol.* **9**, 623–629 (2013).
68. Kavokine, N., Netz, R. R. & Bocquet, L. Fluids at the Nanoscale: From Continuum to Subcontinuum Transport. *Annu. Rev. Fluid Mech.* **53**, 377–410 (2021).
69. Rodriguez, F. J. C., Krapp, L. F., Peraro, M. D. & Abriata, L. A. HandMol: Coupling WebXR, AI and HCI technologies for Immersive, Natural, Collaborative and Inclusive Molecular Modeling. 2023.11.24.568613 Preprint at https://doi.org/10.1101/2023.11.24.568613 (2023).
70. Eastman, P. *et al.* OpenMM 7: Rapid development of high performance algorithms for molecular dynamics. *PLOS Comput. Biol.* **13**, e1005659 (2017).
71. Maier, J. A. *et al.* ff14SB: Improving the Accuracy of Protein Side Chain and Backbone Parameters from ff99SB. *J. Chem. Theory Comput.* **11**, 3696–3713 (2015).